Copyright notice

It will be published in the IEEE Signal Processing Letters, volume: 22, Issue: 11, Pages 1864-1868, Nov. 2015, DOI: 10.1109/LSP.2015.2438176.

Physical modeling and performance bounds for device-free localization systems

Vittorio Rampa, *Member, IEEE,* Stefano Savazzi, *Member, IEEE,* Monica Nicoli, *Member, IEEE,* Michele D'Amico *Member, IEEE,*

***Abstract*—In this letter, an analytically tractable model based on diffraction theory is proposed to describe the perturbations of the electromagnetic propagation of radio signals caused by the presence of a moving object in the two dimensional (2-D) area near the transmitting/receiving devices. This novel model is instrumental to the evaluation of non-cooperative device-free localization (DFL) systems as it allows to relate the received signal strength measurements of multiple radio links to the object size, orientation and position. The proposed model is validated experimentally using radio devices and it is used to derive closed-form fundamental limits to DFL accuracy, providing an analytical tool for DFL system design and network 2-D pre-deployment assessment.**

***Index Terms*—Cramer-Rao lower bound, device-free localization, human body shadowing, wireless sensor networks.**

I. Introduction

DEVICE-FREE localization (DFL) [1] of objects or people moving in confined areas covered by a wireless network is made possible as the presence of obstacles affects the radio waves nearby [2], [3] in terms of signal strength in a way that strongly depends on the target position. Without any additional sensor hardware, DFL methods enable the estimation of the target location by simply measuring the received signal strength (RSS) in both static [4] and dynamic [5] environments. In line with the rapidly evolving software-defined radio (SDR) paradigm, the DFL technology is expected to provide a protocol-independent infrastructure that supports sensor-less localization and context recognition services tailored for industrial and smart workspace applications. Despite some recent attempts to model the fading effects induced by moving bodies on short-range radio propagation [6], these mostly addressed inter- [7] and intra-body [8] area communication systems for modeling body-induced propagation losses for narrow [9] or wide-band [10] applications with the purpose of mitigating these effects. Another important topic discussed so far is modeling of body effects for critical network layout optimization [11]. A unified physical model, for the prediction of the correlation between the target location and the corresponding wireless field perturbation, is still controversial as pointed out in [12] or too complex to be of practical use in most scenarios, as based on ray tracing techniques [13] or uniform theory of diffraction [7]. We introduce here a novel and analytically tractable model for prediction of the body-induced propagation loss found in DFL applications, modeling both the dominant static component and the stochastic fluctuations of the power

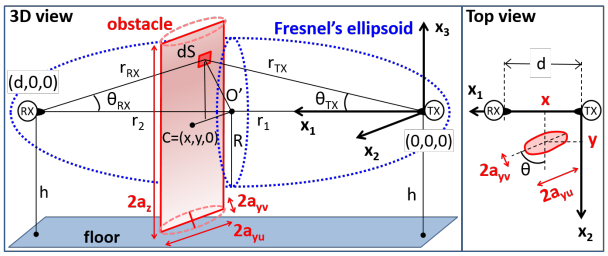

Figure 1. Geometry of the radio-link layout.

loss as a function of the target location. This model, that extends the validity of the one employed in [14], [15] for objects placed only along the line-of-sight (LOS) path, is exploited to analytically compute the Cramer-Rao Lower Bound (CRLB) to evaluate the theoretical limits to localization accuracy over the whole 2-D link area. The propagation loss by body shadowing greatly affects the RSS [16] even when considering a multipath environment where several rays contribute to the received power. Therefore, in this letter, electromagnetic (EM) field perturbations are modeled as a combination of multipath and diffraction terms. The diffraction component, not considered in previous DFL models [12], is defined here in closed form according to the simple knife-edge diffraction theory [17] and embeds information about the target location and size. Instead, multipath fading contributions uniformly impair radio communications for target located inside a link sensitivity area that depends on the link geometry and object size. In [11], the movements of the human body are only considered in predetermined perpendicularly crossing and parallel paths with respect to LOS path, while the human body is approximated by a homogeneous shape and its effects are computed by using ray-tracing techniques. With respect to [15], where the RSS perturbations were measured along the LOS path during a training stage and [14], [18], where large obstacles are placed along the LOS path by exploiting geometrical theory of diffraction methods, the proposed model is able to predict the induced power loss for any target (i.e., small or large) placed in the 2-D area surrounding the link. Experimental results confirm that the model can effectively capture the relationship between the target position and the link RSS.

II. Diffraction models for DFL

We assume a radio link arranged in the 3-D space (x_1, x_2, x_3) as in Fig. 1. The target is modeled as a perfectly EM absorbing rectangular 2-D surface [14] that is orthogonally placed w.r.t. the LOS segment connecting the transmitter (TX)

and receiver (RX). In the literature [17], 2-D diffraction is widely used to make deterministic prediction of diffraction losses. This approach shows reasonably good results even if the 2-D approximation of a generic 3-D target ignores important parameters such as polarization, permittivity/conductivity values, surface roughness, thickness and shape [19]. The link is located at distance h from the floor without walls or ceiling and the corresponding Fresnel's ellipsoid [14] does not have any contact with the other parts of the scenario except for the aforementioned target: $h > \sqrt{\lambda d}/2$ where λ is the wavelength while d is the RX-TX distance. According to standard short-range propagation models [20], ground reflections are ignored, too. The target barycenter is located in $\mathbf{X} = [x, y]^T$ in the 2-D horizontal space, with off-axis displacement y. The target can assume any orientation $\theta \in [-\pi, \pi]$ w.r.t. the LOS (i.e., the object/person can turn while standing in $\mathbf{X}$). The 3-D body shows an equivalent 2-D surface S_{obs} having height $2a_z$ and width $2a_y$, where the semi-size $a_y = a_y(\theta) \in [a_{yv}, a_{yu}]$ changes w.r.t. θ with $a_{yv} = \min_\theta[a_y(\theta)]$ and $a_{yu} = \max_\theta[a_y(\theta)]$.

The electric field at the RX can be predicted as generated by a virtual array of Huygens' sources located on the obstacle plane and not belonging to the obstacle itself. The electric field dE due to the diffraction effects caused by the elementary Huygens' source of area $dS = dx_2 dx_3$ having generic coordinates (x_1, x_2, x_3) is given in [14] as

$$dE = \frac{1}{2} j E_0 \exp\left(-j\frac{\pi}{2}u_2^2\right) \exp\left(-j\frac{\pi}{2}u_3^2\right) du_2 du_3, \quad (1)$$

where E_0 is the electric field at the RX due to the TX when no obstacle is present. The following variable substitutions are used: $u_2 = \sqrt{2}\, x_2/R$ and $u_3 = (x_3/x_2) \cdot u_2$ where $R = \sqrt{\lambda r_1 r_2/(r_1 + r_2)}$ is the Fresnel's radius and r_1, r_2 the distances w.r.t. the TX and RX, respectively. Eq. (1) is valid when hypotheses $\max\{|x_2|, |x_3|, \lambda\} \ll \min\{r_1, r_2\}$, $\cos\theta_{TX} \simeq 1$ and $\cos\theta_{RX} \simeq 1$ hold true. These are realistic assumptions for the target positioned on, or nearby, the LOS (i.e, for small enough y) and wavelength much smaller than the distances r_1, r_2. By using (1), the electric field E_1 at the RX is $E_1 = E_0 - \int_{S_{\text{obs}}} dE$ [18], while through the Fresnel cosine $C(\xi)$ and sine $S(\xi)$ integrals [21] we get the electric field ratio $|E/E_0|^2 = \mathrm{G}(\mathbf{X}|\, a_y, a_z)$ as

$$\mathrm{G}(\mathbf{X}|\, a_y, a_z) = 1 + (C_z^2 + S_z^2)(\Gamma_C^2 + \Gamma_S^2) - 2C_z\Gamma_C - 2S_z\Gamma_S \quad (2)$$

where $C_z = C\left(\frac{a_z}{R/\sqrt{2}}\right)$, $S_z = S\left(\frac{a_z}{R/\sqrt{2}}\right)$, $\Gamma_C = C\left(\frac{y+a_y}{R/\sqrt{2}}\right) - C\left(\frac{y-a_y}{R/\sqrt{2}}\right)$ and $\Gamma_S = S\left(\frac{y+a_y}{R/\sqrt{2}}\right) - S\left(\frac{y-a_y}{R/\sqrt{2}}\right)$. $\mathrm{G}(\mathbf{X}|a_y, a_z)$ depends on the position $\mathbf{X}$ and on the physical dimensions of the obstacle $a_y = a_y(\theta)$ and a_z. For tall objects (i.e., $a_z \gg R$) placed near the LOS (i.e., $|y| < a_y$), an approximation of (2) is found by using the asymptotic approximations [21] for $C(\xi)$ and $S(\xi)$ (i.e., for $\xi \gg 1$) as

$$\mathrm{G}(\mathbf{X}|a_y) \simeq \left[\frac{R}{\pi a_y}\cos(2\pi f_y y)\right]^2, \ \forall \mathbf{X} \in \mathcal{H}_{\mathrm{W},d} \quad (3)$$

with spatial frequency $f_y = a_y/R^2$ and $\mathcal{H}_{\mathrm{W},d} \triangleq \left\{\mathbf{X} \in \mathcal{H}_{\mathrm{W},d} : 0 \le x \le d,\ |y| \le \frac{1}{2}\mathrm{W}(x)\right\}$ with $\mathrm{W}(x) = 1/f_y = \lambda x(d-x)/a_y d$. This approximation captures the physical effects of an obstructing target located inside the link sensitivity area $\mathcal{H}_{\mathrm{W},d}$ where the target influences the RF field. This area is an eye-shaped zone centered on the LOS, with length d and width $\mathrm{W}(x)$ varying with x (see Sect. IV). This novel result extends the validity of the approximation adopted in [15], [14] including not only the LOS (i.e., $y = 0$) but also the area near the LOS (i.e., $|y| \le \frac{1}{2}\mathrm{W}(x)$). The approximation (3) overestimates the true field ratio along the LOS and can be safely used only for tall obstacles that have semi-size $a_y > R$.

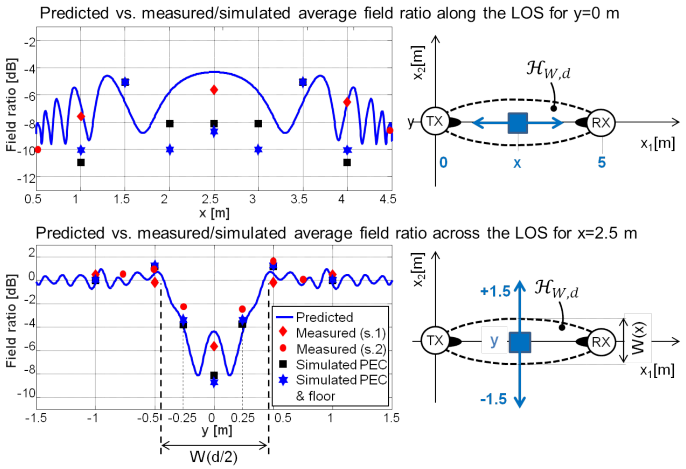

Figure 2. Predicted average field ratio along and across the LOS path. Measurements and PEC simulations are superimposed for comparison.

III. Stochastic Modeling of Human-Induced Fading

Assuming that the RX can measure the perturbation $\mathrm{G}(\mathbf{X}|a_y(\theta), a_z)$ according to (2) by observing the received signal power P, the aim of this section is to introduce an analytically tractable model that relates P to the location $\mathbf{X}$ and use it for localization of the target in DFL systems. The RSS measurement P, in logarithmic scale, observed over the link sensitivity area $\mathcal{H}_{\mathrm{W},d}$ can be modeled as a Gaussian random variable [22]

$$P = \begin{cases} \mathcal{P}_0 = h_0 + w_0, & \mathbf{X} \notin \mathcal{H}_{\mathrm{W},d} \\ \mathcal{P}_1 = h_1(\mathbf{X}, \theta) + w_1, & \mathbf{X} \in \mathcal{H}_{\mathrm{W},d} \end{cases} \quad (4)$$

where $P = \mathcal{P}_0$ and $P = \mathcal{P}_1$ refer to the case of $\mathbf{X}$ being outside (i.e., empty scenario) or inside the link sensitivity area $\mathcal{H}_{\mathrm{W},d}$, respectively. The first term h_0 is a constant that depends only on the geometry of the scenario and on the propagation coefficients [18] while the second term is $h_1(\mathbf{X}, \theta) = \mathrm{G}(\mathbf{X}|a_y(\theta), a_z)|_{\text{dB}} + h_0$ with $\mathrm{G}(\mathbf{X}|a_y(\theta), a_z)$ as in (2); $(\cdot)|_{\text{dB}}$ denotes the linear-to-dB conversion operator. The randomness of measurements and the other scattering effects found in the empty scenario are modeled by the Gaussian disturbance $w_0 \sim \mathcal{N}(0, \sigma_0^2)$ with zero mean and variance σ_0^2. Multipath fading and other random effects, not included in the diffraction model (2) but dependent on the target presence in $\mathcal{H}_{\mathrm{W},d}$, are modeled by the Gaussian noise $w_1 \sim \mathcal{N}(\Delta h_{\mathrm{C}}, \sigma_0^2 + \Delta\sigma_C^2)$ with Δh_{C} and $\Delta\sigma_C^2$ being the residual stochastic multipath fading terms [15].

The target-induced perturbations are evaluated in terms of the average path-loss and power fluctuations assuming that the target is standing in $\mathbf{X}$ with varying orientation θ. To this aim, the RSS mean and the variance are computed by averaging over the azimuth θ. In case of target being outside $\mathcal{H}_{\mathrm{W},d}$, the RSS mean and variance are $\mu_0 = \mathrm{E}_{w_0}[\mathcal{P}_0] = h_0$ and $\sigma_0^2 = \mathrm{Var}_{w_0}[\mathcal{P}_0]$, respectively. These terms can be evaluated from measurements performed during the calibration phase when the link area does not contain any target. On the contrary, the target presence modifies both the mean $\mu_1(\mathbf{X}) = \mathrm{E}_{\theta,w_1}[\mathcal{P}_1]$ and variance $\sigma_1^2(\mathbf{X}) = \mathrm{Var}_{\theta,w_1}[\mathcal{P}_1]$ according to

$$\mu_1(\mathbf{X}) = h_0 + \underbrace{\Delta h_C + \mathrm{E}_\theta\left[\mathrm{G}(\mathbf{X}|a_y(\theta),a_z)|_{\mathrm{dB}}\right]}_{\Delta\mu(\mathbf{X})} \quad (5)$$

$$\sigma_1^2(\mathbf{X}) = \sigma_0^2 + \underbrace{\Delta\sigma_C^2 + \mathrm{Var}_\theta\left[\mathrm{G}(\mathbf{X}|a_y(\theta),a_z)|_{\mathrm{dB}}\right]}_{\Delta\sigma^2(\mathbf{X})} \quad (6)$$

where the RSS average $\Delta\mu(\mathbf{X}) = \mu_1(\mathbf{X}) - \mu_0$ and variance $\Delta\sigma^2(\mathbf{X}) = \sigma_1^2(\mathbf{X}) - \sigma_0^2$ increments are highlighted. Perturbations of the RSS average and variance in (5)-(6) are therefore due to a combination of multipath reflections and diffraction effects. As confirmed by the results of Sect. III-A, the multipath terms Δh_C and $\Delta\sigma_C^2$ do not depend on the object position [22] and can be easily estimated from measurements during the calibration phase (i.e., they are not relevant for localization). On the other hand, the diffraction term $\mathrm{G}(\mathbf{X}|\cdot)|_{\mathrm{dB}}$ provides a simple but effective tool to predict the power perturbation as a function of the target position and size. For the sake of simplicity, here we approximate the expectations in (5)-(6) by assuming that the target orientation can only take its extreme values $\{a_{yv}, a_{yu}\}$ with equal probabilities $\Pr(a_y(\theta) = a_{yv}) = \Pr(a_y(\theta) = a_{yu}) = 1/2$. Under these assumptions, $\Delta\mu(\mathbf{X})$ and $\Delta\sigma^2(\mathbf{X})$ can be expressed as

$$\Delta\mu(\mathbf{X}) = \Delta h_C + 5\log_{10}\left[\mathrm{G}_u(\mathbf{X})\cdot\mathrm{G}_v(\mathbf{X})\right] \quad (7)$$

$$\Delta\sigma^2(\mathbf{X}) = \Delta\sigma_{\mathrm{C}}^2 + \left(5\log_{10}\left[\frac{\mathrm{G}_u(\mathbf{X})}{\mathrm{G}_v(\mathbf{X})}\right]\right)^2 \quad (8)$$

with $\mathrm{G}_u(\mathbf{X}) = \mathrm{G}(\mathbf{X}|a_y,a_z)|_{a_y=a_{yu}}$, $\mathrm{G}_v(\mathbf{X}) = \mathrm{G}(\mathbf{X}|a_y,a_z)|_{a_y=a_{yv}}$ and $\mathrm{G}(\mathbf{X}|a_y,a_z)$ defined in (2). The sensitivity area $\mathcal{H}_{\mathrm{W},d}$ depends on $a_y(\theta)$ and therefore on θ, too. However, following the same approach of (5) and (6), for $\mu_1(\mathbf{X})$ and $\sigma_1^2(\mathbf{X})$ respectively, the equivalent semi-size $a_y(\theta) \simeq a_{ye} = \sqrt{a_{yu}a_{yv}}$ can be used to produce the same average field ratio caused by the moving target.

A. Model calibration and validation

To validate the model of Sect. II, several RF experiments and EM simulations have been carried out as summarized in Fig. 2. Each RF test consists of two sets of RSS measurements performed in a large hall. RSS data are acquired by pre-calibrated SDR devices (USRP N210) equipped with 2 dBi vertical monopole antennas and using a single unmodulated carrier waveform at frequency $f_c = 2.486$ GHz. The first data set is collected with no target to compute the reference values μ_0 and σ_0^2. The second data set corresponds to a target located inside the link sensitivity area. Two experimental tests have been conducted (s.1 and s.2 in Fig. 2). For both tests, the obstacle has maximum and minimum semi-sizes $a_{yu} = 0.275$ m, $a_{yv} = 0.12$ m ($a_{ye} = 0.182$ m) while $a_z = 0.9$ m; the same link-dependent parameters are used: $\Delta\sigma_C^2 = 1$ dB, $\Delta h_C = 0$ dB, $h = 0.9$ m and $d = 5$ m. RF data are collected to obtain $\mu_1(\mathbf{X})$ and $\sigma_1^2(\mathbf{X})$ for some known position $\mathbf{X}$, along and near the LOS. Fig. 2 shows the measured and predicted values of the average RSS increase $\Delta\mu(\mathbf{X})$, according to (7), for target located along the LOS (on top, for $\mathbf{X} = [x,0]^{\mathrm{T}}$) and for target traversing the LOS (at bottom, for $\mathbf{X} = [d/2,y]^{\mathrm{T}}$). Fig. 2 compares also the results of the EM simulations obtained with the commercial software tool FEKO. In this case, a 2-D perfect electric conductor (PEC) surface is used instead of the absorbing one defined in Sect. II but with the same physical dimensions as in Fig. 1. Two scenarios are simulated: *i*) 2-D PEC obstacle over a concrete floor (i.e., an infinite homogeneous semi-space placed below the link at distance h, with EM parameters $\epsilon_r = 5$ and $\tan\delta = 0.14$) and *ii*) 2-D PEC obstacle without floor. With respect to the measured values, the extra attenuation induced by the PEC obstacle is apparent due to the different composition of the obstacle, while the diffraction model (2) better approximates the effects of the human body.

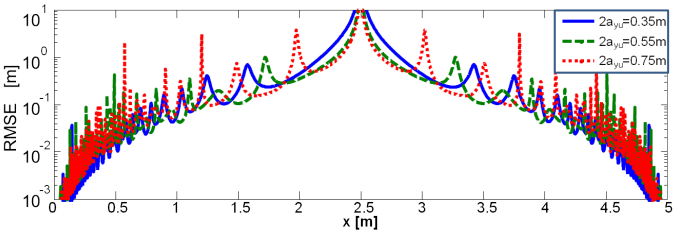

Figure 3. CRLB to the location accuracy $\mathrm{RMSE}_1(\mathbf{X})$ vs. the target coordinate x, for a target located along the LOS ($\mathbf{X} = [x,0]^{\mathrm{T}}$) with different dimensions.

IV. Performance Bounds to Positioning Accuracy

We consider the estimation of the target position $\mathbf{X}$ from the RSS observations P_ℓ over L links by exploiting the knowledge of the mean and variance functions $\{\mu_{1,\ell}(\mathbf{X}), \sigma_{1,\ell}(\mathbf{X})\}$ $\forall\ell = 1,\ldots,L$, as defined in (5)-(6). The maximum positioning accuracy, that can be reached by any unbiased localization algorithm, is evaluated using the CRLB approach. The likelihood function $\mathcal{L}_\ell(\mathbf{X}) = \mathrm{p}(P_\ell|\mathbf{X})$ of the ℓ-th link is

$$\mathcal{L}_\ell(\mathbf{X}) = \frac{1}{\sqrt{2\pi\sigma_{1,\ell}^2(\mathbf{X})}}\exp\left\{-\frac{(P_\ell - \mu_{1,\ell}(\mathbf{X}))^2}{2\sigma_{1,\ell}^2(\mathbf{X})}\right\}. \quad (9)$$

Assuming that the L power measurements are independent, the joint log-likelihood function is $\ln\mathcal{L}(\mathbf{X}) = \sum_{\ell=1}^{L}\ln\mathcal{L}_\ell(\mathbf{X})$. The CRLB matrix $\mathbf{C}(\mathbf{X}) = [C_{i,j}]$ provides a lower bound to the covariance matrix for any unbiased estimator $\hat{\mathbf{X}} = [\hat{x},\hat{y}]^{\mathrm{T}}$ of the target position $\mathbf{X}$ [23] as $\mathrm{E}[(\hat{\mathbf{X}}-\mathbf{X})(\hat{\mathbf{X}}-\mathbf{X})^{\mathrm{T}}] \geq \mathbf{C}(\mathbf{X}) = \mathbf{F}^{-1}(\mathbf{X})$. The Fisher Information Matrix (FIM) $\mathbf{F}(\mathbf{X}) = [F_{i,j}]$ $(i,j = 1,2)$ has elements defined as $F_{i,j} =$

$$\frac{\partial \mathrm{G}}{\partial R} = -\frac{2}{R}\left\{\left[C_z^2+S_z^2\right]\left[\Gamma_C\Lambda_C+\Gamma_S\Lambda_S\right]-C_z\Lambda_C-S_z\Lambda_S-\frac{a_z}{R/\sqrt{2}}[\dot{C}_z\Gamma_C+\dot{S}_z\Gamma_S-(C_z\dot{C}_z+S_z\dot{S}_z)(\Gamma_C^2+\Gamma_S^2)]\right\} \quad (13)$$

$\mathrm{E}\left[\left(\sum_{\ell=1}^{L}\frac{\partial \ln \mathcal{L}_\ell(\mathbf{X})}{\partial x_i}\right)\left(\sum_{\ell=1}^{L}\frac{\partial \ln \mathcal{L}_\ell(\mathbf{X})}{\partial x_j}\right)\right]$. According to (9), the FIM entries are

$$F_{i,j}=\sum_{\ell=1}^{L}\frac{\frac{\partial \mu_{1,\ell}(\mathbf{X})}{\partial x_i}\frac{\partial \mu_{1,\ell}(\mathbf{X})}{\partial x_j}+2\frac{\partial \sigma_{1,\ell}(\mathbf{X})}{\partial x_i}\frac{\partial \sigma_{1,\ell}(\mathbf{X})}{\partial x_j}}{\sigma_{1,\ell}^2(\mathbf{X})}. \quad (10)$$

By differentiation with respect to the target coordinates $x_1 = x$ and $x_2 = y$, and using (7)-(8) with $\mathrm{G}_u(\mathbf{X})$ and $\mathrm{G}_v(\mathbf{X})$ defined as in Sect. III, it is

$$\begin{aligned}
\frac{\partial \mu_{1,\ell}(\mathbf{X})}{\partial x} &= \frac{\alpha}{\mathrm{G}_u\mathrm{G}_v}\left[\frac{\partial \mathrm{G}_u}{\partial R}\mathrm{G}_v+\frac{\partial \mathrm{G}_v}{\partial R}\mathrm{G}_u\right]\frac{\partial R}{\partial x}\\
\frac{\partial \mu_{1,\ell}(\mathbf{X})}{\partial y} &= \frac{\alpha}{\mathrm{G}_u\mathrm{G}_v}\left[\frac{\partial \mathrm{G}_u}{\partial y}\mathrm{G}_v+\frac{\partial \mathrm{G}_v}{\partial y}\mathrm{G}_u\right]\\
\frac{\partial \sigma_{1,\ell}(\mathbf{X})}{\partial x} &= \begin{cases}\frac{\alpha}{\mathrm{G}_u\mathrm{G}_v}\left[\frac{\partial \mathrm{G}_u}{\partial R}\mathrm{G}_v-\frac{\partial \mathrm{G}_v}{\partial R}\mathrm{G}_u\right]\frac{\partial R}{\partial x} & \text{if } \frac{\mathrm{G}_u}{\mathrm{G}_v}\geq 1\\ \frac{\alpha}{\mathrm{G}_u\mathrm{G}_v}\left[\frac{\partial \mathrm{G}_v}{\partial R}\mathrm{G}_u-\frac{\partial \mathrm{G}_u}{\partial R}\mathrm{G}_v\right]\frac{\partial R}{\partial x} & \text{if } \frac{\mathrm{G}_u}{\mathrm{G}_v}<1\end{cases}\\
\frac{\partial \sigma_{1,\ell}(\mathbf{X})}{\partial y} &= \begin{cases}\frac{\alpha}{\mathrm{G}_u\mathrm{G}_v}\left[\frac{\partial \mathrm{G}_u}{\partial y}\mathrm{G}_v-\frac{\partial \mathrm{G}_v}{\partial y}\mathrm{G}_u\right] & \text{if } \frac{\mathrm{G}_u}{\mathrm{G}_v}\geq 1\\ \frac{\alpha}{\mathrm{G}_u\mathrm{G}_v}\left[\frac{\partial \mathrm{G}_v}{\partial y}\mathrm{G}_u-\frac{\partial \mathrm{G}_u}{\partial y}\mathrm{G}_v\right] & \text{if } \frac{\mathrm{G}_u}{\mathrm{G}_v}<1\end{cases}
\end{aligned} \quad (11)$$

with $\alpha=\frac{5}{\ln 10}$ and $\frac{\partial R}{\partial x}=\frac{\lambda}{2R}\left(1-\frac{2x}{d}\right)$. The partial derivatives $\frac{\partial \mathrm{G}}{\partial R}$, $\frac{\partial \mathrm{G}}{\partial y}$ are shown in (12)-(13) with definitions as in (2)

$$\frac{\partial \mathrm{G}}{\partial y}=\frac{2\sqrt{2}}{R}\left\{\left[C_z^2+S_z^2\right]\left[\Gamma_C\dot{\Gamma}_C+\Gamma_S\dot{\Gamma}_S\right]-C_z\dot{\Gamma}_C-S_z\dot{\Gamma}_S\right\} \quad (12)$$

with $\Lambda_C=\frac{y+a_y}{R/\sqrt{2}}\dot{C}\left(\frac{y+a_y}{R/\sqrt{2}}\right)-\frac{y-a_y}{R/\sqrt{2}}\dot{C}\left(\frac{y-a_y}{R/\sqrt{2}}\right)$, $\Lambda_S=\frac{y+a_y}{R/\sqrt{2}}\dot{S}\left(\frac{y+a_y}{R/\sqrt{2}}\right)-\frac{y-a_y}{R/\sqrt{2}}\dot{S}\left(\frac{y-a_y}{R/\sqrt{2}}\right)$ and $\dot{F}(\xi)$ being the first derivative of the generic $F(\xi)$. By substituting (11) into (10), it is straightforward to obtain $\mathbf{F}(\mathbf{X})$ and then $\mathbf{C}(\mathbf{X})$.

The CRLB matrix is numerically evaluated to analyze the localization accuracy in term of Root Mean Square Error (RMSE) of the position estimate along the two spatial coordinates, $\mathrm{RMSE}_1(\mathbf{X})=\sqrt{E[(\hat{x}-x)^2]}\geq\sqrt{C_{11}}$ and $\mathrm{RMSE}_2(\mathbf{X})=\sqrt{E[(\hat{y}-y)^2]}\geq\sqrt{C_{22}}$, and the overall 2-D position accuracy $\mathrm{RMSE}(\mathbf{X})=\sqrt{E[|\hat{\mathbf{X}}-\mathbf{X}|^2]}\geq\sqrt{\mathrm{C}_{11}+\mathrm{C}_{22}}$. The single link ($L=1$) CRLB is shown in Fig. 3-4 for an obstacle with the same size as in Sect. III-A. In Fig. 3, the lower bound to $\mathrm{RMSE}_1(\mathbf{X})$ is shown for a target located along the LOS ($y=0$). Different dimensions of the target are also considered to highlight their effects on the CRLB: in the central part of the LOS path (i.e., between 2 and 3 m) large obstacles give better positioning accuracy than smaller ones. Outside this zone, there are large CRLB fluctuations even if, in practice, the observed accuracy is comparable. In Fig. 5, the limit to the position accuracy $\mathrm{RMSE}(\mathbf{X})$ is evaluated for different positions $\mathbf{X}$. As expected, the localization accuracy is highly space-varying: the model predicts a higher sensing capability of the radio link near the TX and RX, compared to the sensitivity that is observed for targets located in-between. The localization accuracy is reasonably high when the target is near the TX and the RX: e.g., the CRLB is 6cm for $\mathbf{X}=[25,\pm 5]$ cm and $\mathbf{X}=[475,\pm 5]$ cm. For target in-between, the reduced sensitivity may be counter-balanced by improving the multiplicity of the links, as in the 4-node ($L=2$) layout of Fig. 5 where the CRLB for $\mathbf{X}=[2,\pm 7.5]$ cm is 43.4 cm for $L=2$ while it is >2 m for $L=1$.

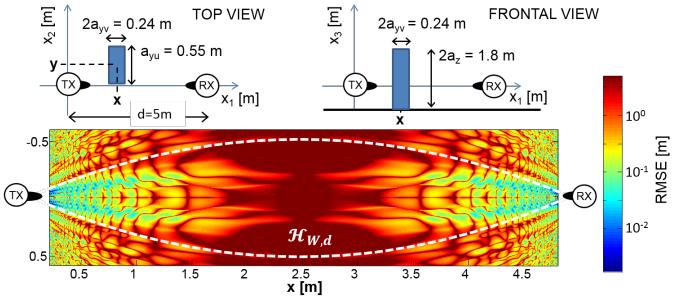

Figure 4. CRLB to the positioning accuracy $\mathrm{RMSE}(\mathbf{X})$ vs. the target location $\mathbf{X}=[x,y]^{\mathrm{T}}$ for the single link topology. The area $\mathcal{H}_{\mathrm{W},d}$ is highlighted.

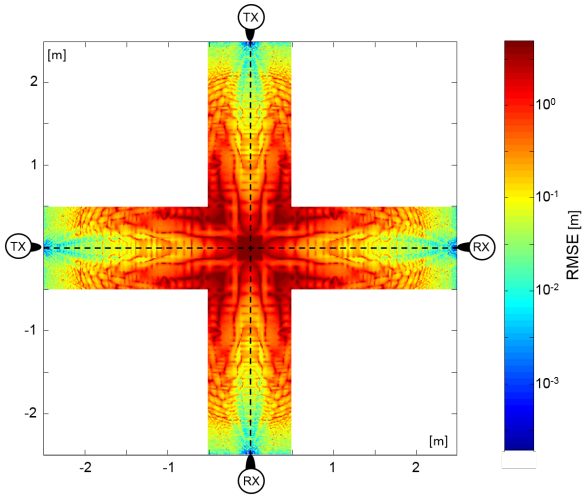

Figure 5. CRLB to the positioning accuracy $\mathrm{RMSE}(\mathbf{X})$ vs. the target location $\mathbf{X}=[x,y]^{\mathrm{T}}$ for a 4-node (2x2: 2 TX, 2 RX) network topology.

V. Conclusions

An ad-hoc physical model, based on the EM diffraction theory, has been proposed to describe the fluctuations of the radio signal caused by the presence of a target between the transmitter and receiver. The model, that has been validated experimentally by several indoor field tests, relates the RSS measurements to the target size, orientation and position. Closed-form derivation of the CRLB has been obtained for single and multi-link scenarios as a pre-deployment predictor of the localization accuracy.

References

[1] M. Youssef, M. Mah, and A. Agrawala, "Challenges: Device-free passive localization for wireless environments," in *Proceedings of the 13th Annual ACM International Conference on Mobile Computing and Networking (MobiCom '07)*. ACM, 2007, pp. 222–229.

[2] K. Woyach, D. Puccinelli, and M. Haenggi, "Sensorless sensing in wireless networks: Implementation and measurements," in *Proceedings of the 4th International Symposium on Modeling and Optimization in Mobile, Ad Hoc and Wireless Networks*, April 2006, pp. 1–8.
[3] N. Patwari and J. Wilson, "RF Sensor Networks for Device-Free Localization: Measurements, Models, and Algorithms," *Proceedings of the IEEE*, vol. 98, no. 11, pp. 1961–1973, Nov 2010.
[4] M. Seifeldin, A. Saeed, A. Kosba, A. El-Keyi, and M. Youssef, "Nuzzer: A large-scale device-free passive localization system for wireless environments," *IEEE Transactions on Mobile Computing*, vol. 12, no. 7, pp. 1321–1334, July 2013.
[5] A. Saeed, A. Kosba, and M. Youssef, "Ichnaea: A low-overhead robust wlan device-free passive localization system," *IEEE Journal of Selected Topics in Signal Processing*, vol. 8, no. 1, pp. 5–15, Feb 2014.
[6] M. Cheffena, "Physical-statistical channel model for signal effect by moving human bodies,," *EURASIP Journal on Wireless Communications and Networking*, no. 77, pp. 1–13, Jan 2012.
[7] G. Koutitas, "Multiple human effects in body area networks," *IEEE Antennas and Wireless Propagation Letters*, vol. 9, pp. 938–941, 2010.
[8] N. Cho, J. Yoo, S.-J. Song, J. Lee, S. Jeon, and H.-J. Yoo, "The human body characteristics as a signal transmission medium for intrabody communication," *IEEE Transactions on Microwave Theory and Techniques*, vol. 55, no. 5, pp. 1080–1086, May 2007.
[9] Y. Nechayev, P. Hall, and Z. Hu, "Characterisation of narrowband communication channels on the human body at 2.45 ghz," *IET Microwaves Antennas Propagation*, vol. 4, no. 6, pp. 722–732, June 2010.
[10] A. Fort, J. Ryckaert, C. Desset, P. De Doncker, P. Wambacq, and L. Van Biesen, "Ultra-wideband channel model for communication around the human body," *IEEE Journal on Selected Areas in Communications*, vol. 24, no. 4, pp. 927–933, April 2006.
[11] M. Ghaddar, L. Talbi, T. Denidni, and A. Sebak, "A conducting cylinder for modeling human body presence in indoor propagation channel," *Antennas and Propagation, IEEE Transactions on*, vol. 55, no. 11, pp. 3099–3103, Nov 2007.
[12] B. Hamilton, M. Xiaoli, R. Baxley, and S. Matechik, "Propagation modeling for radio frequency tomography in wireless networks," *IEEE Journal of Selected Topics in Signal Processing*, vol. 8, no. 1, pp. 55–65, Feb 2014.
[13] A. Eleryan, M. Elsabagh, and Y. M., "Synthetic generation of radio maps for device-free passive localization," in *Proceedings of the IEEE Global Telecommunication Conference (GLOBECOM 2011)*, Dec 2011, pp. 1–5.
[14] H. Mokhtari and P. Lazaridis, "Comparative study of lateral profile knife-edge diffraction and ray tracing technique using gtd in urban environment," *IEEE Transactions on Vehicular Technology*, vol. 48, no. 1, pp. 255–261, Jan 1999.
[15] S. Savazzi, M. Nicoli, F. Carminati, and M. Riva, "A Bayesian approach to Device-Free Localization: Modeling and experimental assessment," *IEEE Journal of Selected Topics in Signal Processing*, vol. 8, no. 1, pp. 16–29, Feb 2014.
[16] S. Obayashi and J. Zander, "A body-shadowing model for indoor radio communication environments," *IEEE Transactions on Antennas and Propagation*, vol. 46, no. 6, pp. 920–927, Jun 1998.
[17] G. Durgin, "The practical behavior of various edge-diffraction formulas," *IEEE Antennas and Propagation Magazine*, vol. 51, no. 3, pp. 24–35, June 2009.
[18] R. Luebbers, "Finite conductivity uniform gtd versus knife edge diffraction in prediction of propagation path loss," *IEEE Transactions on Antennas and Propagation*, vol. 32, no. 1, pp. 70–76, Jan 1984.
[19] B. Davis and G. Brown, "Diffraction by a randomly rough knife edge," *IEEE Transactions on Antennas and Propagation*, vol. 50, no. 12, pp. 1769–1778, Dec 2002.
[20] ITU-R, "Recommendation ITU-R P.1411-6," Propagation data and prediction methods for the planning of short-range outdoor radiocommunication systems and radio local area networks in the frequency range 300 MHz to 100 GHz, P Series Radiowave propagation, Feb 2012.
[21] M. Abramovitz and I. Stegun, "Handbook of mathematical functions," Applied mathematics series 55, Cap. 7, 1972.
[22] A. Coulson, A. Williamson, and R. Vaughan, "A statistical basis for lognormal shadowing effects in multipath fading channels," *IEEE Transactions on Communications*, vol. 46, no. 4, pp. 494–502, Apr 1998.
[23] S. Kay, "Fundamentals of statistical signal processing: Estimation theory," Prentice Hall, 1993.